

High-Performance AlGa_xN-Based Solar-Blind UV Photodetectors for Sensing Applications

Yiping Chen, Chaohong Zheng, and Yiren Chen*

The full solid-state, intrinsic cutoff solar-blind UV photodetectors are widely used in the military and civilian fields. Herein, to achieve real-time solar-blind UV signal detection for application in portable equipment, the material epitaxy, device fabrication, and performance characterization of high-performance back-illuminated AlGa_xN-based solar-blind UV photodetectors are conducted at first. Based on the photodetector, a discrete signal amplifier circuit is subsequently designed and prepared to fulfill the weak solar-blind signal detection. Through assembling the amplifier circuit with the AlGa_xN-based solar-blind UV photodetector, it can output real-time voltage signal with different amplitude according to the intensity of the incident UV light signal. This study is of great significance for developing a portable solar-blind UV detection system.

1. Introduction

In addition to the fields of deep UV light-emitting diodes (LEDs)^[1–4] and laser diodes (LDs),^[5–7] AlGa_xN-based material has drawn much attention for developing full solid-state, intrinsic cutoff wavelength solar-blind UV photodetectors because of their direct, wide, and tunable energy bandgap. The AlGa_xN-based solar-blind UV photodetectors have an extremely extensive application prospect in missile approach warning systems (MAWS) for both important military and civilian targets, corona leakage detection for ultrahigh voltage (UHV) power transmission networks, real-time UV radiation monitoring for wearable or portable devices, environment monitoring for human society, and so on.^[8,9] However, due to the lattice and thermal mismatch between the AlGa_xN and the underlying substrate under existing mainstream heteroepitaxial growth methods, the large density of defects, e.g., point defects, screw dislocations, and edge dislocations, have hindered the performances of AlGa_xN-based solar-blind UV photodetectors. The recent achievements about the

preparation of high-quality AlN templates as ideal substrates^[8,10,11] and the optimal design of the detector structure^[9,12] are expected to overcome the problem.


In this work, a high-performance AlGa_xN-based solar-blind UV photodetector is first fabricated to realize real-time environmental solar-blind UV radiation sensing application for portable devices, and then a discrete signal amplifier circuit is designed to fulfill weak signal detection.

2. Results and Discussion

The typical (0002)-plane symmetrical RSM of the epilayer is shown in **Figure 1c**, mainly including diffraction peaks of AlN, SLs, AlGa_xN, and Al_xGa_{1-x}N gradient layers. The detailed reciprocal lattice points (RLPs) are shown in the asymmetrical RSM around (10 $\bar{1}$ 5) reflection (**Figure 2**). Each one of the RLPs is well consistent with the schematic structure of **Figure 1a**, wherein, q_x and q_z are the directions parallel and perpendicular to the layer interface, respectively. The RLP denoted as (q_x , q_z) for AlN is (−3.709, 10.037), which is almost consistent with the unstrained bulk AlN of (−3.71, 10.037).^[13,14] This means that the AlN layer in this article is almost relaxed. As shown in **Figure 1c**, the black arrowed line extended from (−3.71, 10.037) of the fully relaxed AlN to (−3.62, 9.642) of the fully relaxed GaN represents the fully relaxed Al_xGa_{1-x}N. It should be noted that the RLP of fully relaxed GaN is beyond the coordinates. The right side of the black arrow line represents Al_xGa_{1-x}N suffering tensile strain, while its left side is under compressive strain.^[15] Thus, the RLPs of Al_{0.64}Ga_{0.36}N/AlN SLs layer and the i-Al_{0.64}Ga_{0.36}N layer (I) located at the left side of the strain boundary indicate their subjection to compressive strain. However, the RLP of n-Al_{0.62}Ga_{0.38}N layer (II) located at the right side close to the black arrow line indicates the slight tensile strain in it, which is quite in agreement with the strain modulation effect of Si doping in AlGa_xN revealed by Cantu et al.^[16] The RLP of the i-Al_{0.46}Ga_{0.54}N layer (IV) located at the black arrow line indicates its full relaxation, which can be ascribed to the strain regulation effect of a thin n-Al_xGa_{1-x}N gradient layer (III) (marked by yellow ellipse) introduced as a transition layer between n-Al_{0.62}Ga_{0.38}N and i-Al_{0.46}Ga_{0.54}N. The final p-Al_xGa_{1-x}N gradient layer (V) presents compressive strain that is beneficial to avoid surface cracking. Moreover, it also plays a role in creating a polarization charge field. It is well accepted that the III-group nitride materials epitaxially grown by MOCVD are more likely to present metal face without special process.^[17,18] Also, it is

Y. Chen, C. Zheng
College of Resource and Environment
Quanzhou Normal University
Quanzhou 362000, China

Y. Chen
State Key Laboratory of Luminescence and Applications
Changchun Institute of Optics, Fine Mechanics and Physics
Chinese Academy of Sciences
Changchun 130033, China
E-mail: chenyr@ciomp.ac.cn

 The ORCID identification number(s) for the author(s) of this article can be found under <https://doi.org/10.1002/pssa.202100207>.

DOI: 10.1002/pssa.202100207

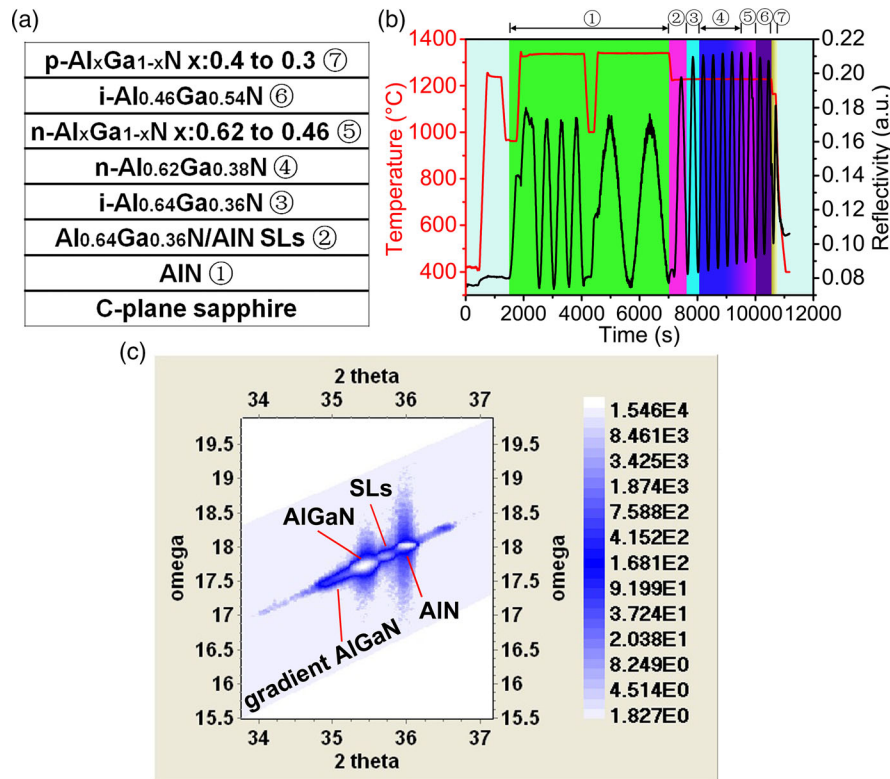


Figure 1. a) Schematic configuration of the PIN structure AlGaIn-based epitaxial material. b) The temperature and 405 nm-wavelength reflectance monitoring curves during growth process. c) The (0002)-plane symmetrical RSM for the epilayer.

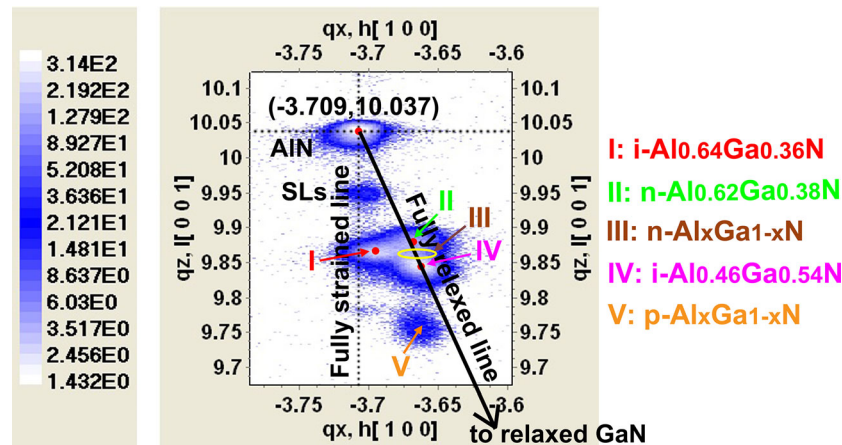


Figure 2. The (10 $\bar{1}5$)-plane asymmetrical RSM for the epilayer.

demonstrated that a positive polarization charge field will be created when the Al-content is gradually changing from GaN to AlGaIn on Ga-face substrate.^[19,20] Oppositely, a negative polarization field can be created when the Al-content is degrading from AlGaIn to GaN. Therefore, when the Al-content of p-Al_xGa_{1-x}N layer linearly changes from 0.4 to 0.3, it results in forming a fixed negative polarization charge field to attract photogenerated hole carriers. As a result, it reduces the loss of photogenerated carriers due to reflection or trapping at abrupt heterojunctions and enhances the performance of the PIN structure AlGaIn-based

solar-blind photodetector by improving the separation, transmission, and collection of carriers.^[9]

Based on the epitaxial material, a back-illuminated AlGaIn-based solar-blind UV photodetector is fabricated by standard optoelectronic processing technology. The process can be referred to in Experimental Section for details. **Figure 3a** shows the schematic and physical images of the device. Its *I*-*V* characteristic curve in dark condition is shown in **Figure 3b**, which presents a good rectifying feature of PN junction. The inset shows the relationship between current density and applied

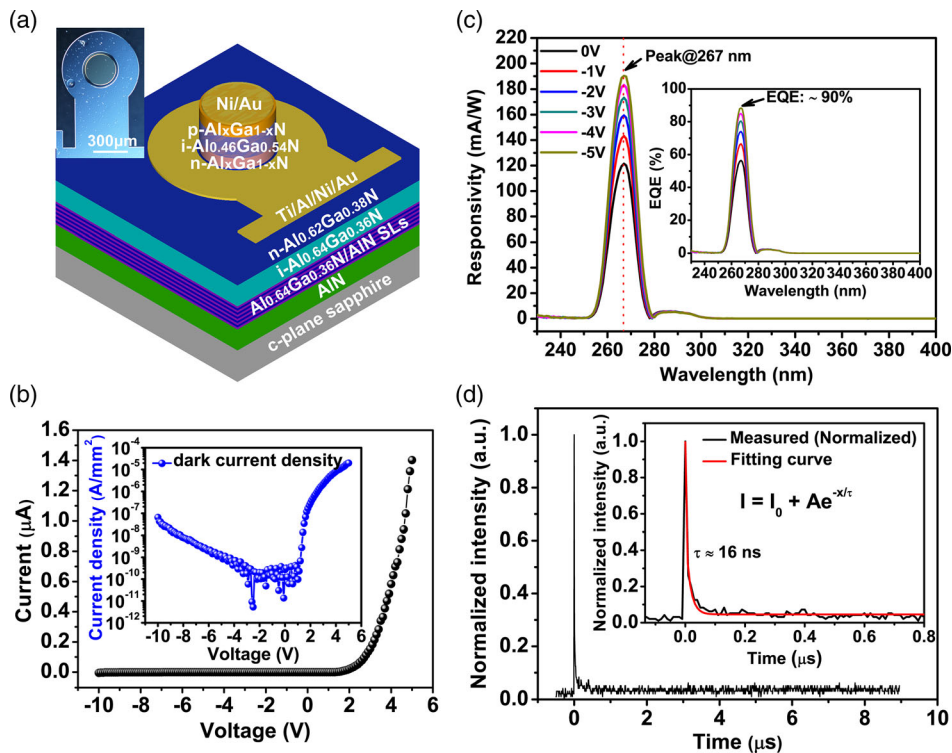


Figure 3. a) Schematic illustration and optical micrograph of the back-illuminated AlGaN-based solar-blind UV photodetector. b) The I - V characteristic curve in dark ambient and its relevant current density (inset) of the physical device. c) The measured spectral responsivities under different bias voltages. The inset shows the corresponding EQEs. d) The normalized transient spectral response under reverse bias voltage of 5 V. The inset shows its first-order exponential decay fitting.

voltage. As can be seen, it shows a low current density (J) of $6.49 \times 10^{-8} \text{ A mm}^{-2}$ at -10 V , although its reverse saturation current density increases with the increase in reverse voltage. The reason for the increase in reverse saturation current density is closely related to the dislocation defects in heteroepitaxial material. It has been reported that the dislocation defects act as current leakage channels in AlGaN-based optoelectronic devices.^[21] It is easy to generate additional leakage current under the applied reverse voltage. Moreover, the leakage current increases with the reverse bias. The spectral performances of the photodetector are also shown in Figure 3c and its inset. The measured response spectra and corresponding external quantum efficiencies (EQEs) under different bias voltages present a bandpass feature ranging from 253 to 280 nm, with peak responsivity and EQE at 267 nm increasing from 121.5 mA W^{-1} and 56.4% for zero-bias to 190.3 mA W^{-1} and $\approx 90\%$ for 5 V reverse bias. The small tail in the response spectrum can be originated from the contribution of the p-Al_xGa_{1-x}N gradient layer. The UV/visible rejection ratio is evaluated to be more than three orders of magnitude. Figure 3d shows the transient response characteristic of the detector under reverse bias voltage of 5 V. The decay section is well fitted by a first-order exponential decay function, as shown in the inset. The response speed is about 16 ns which can be regarded as a good indicator.

To meet the weak signal detection requirement and realize real-time sensing application for portable equipment, an amplifier circuit with high gain and low noise is needed for

the AlGaN-based UV photodetector. Herein, based on the obtained back-illuminated photodetector, the corresponding amplifier circuit is designed and fabricated, as shown in Figure 4. The circuit block diagram is shown in Figure 4a, which is composed of three sections, including preamplifier, emitter follower, and two-stage main amplifier. The schematic circuit diagram can be seen in Figure S1, Supporting Information. To improve the gain stability and reduce the circuit noise, the preamplifier section worked in inverse amplification mode is introduced to provide a strong anti-interference ability. Meanwhile, a T-type resistance feedback network is introduced to realize weak photo-current extraction, which is different from the conventional high-resistance feedback. The weak voltage signal output from the preamplifier will input the emitter follower section. Because the emitter follower has the characteristics of large input impedance and small output impedance, it can reduce the influence on the output signal of preamplifier circuit and play the role of impedance matching to make the postamplifier circuit work better in the intermediate stage. Then, the output signal of the emitter follower will pass through the two-stage main amplifier circuit to further enlarge the voltage signal. In this step, it works in the in-phase amplification mode to ensure the magnification factor of each stage greater than 1 and can be adjusted proportionally by the feedback resistor. Finally, the enlarged output voltage signal is recorded by a commercial data acquisition system. The whole amplifier circuit assembled with an AlGaN-based solar-blind UV photodetector is shown in Figure 4b,c.

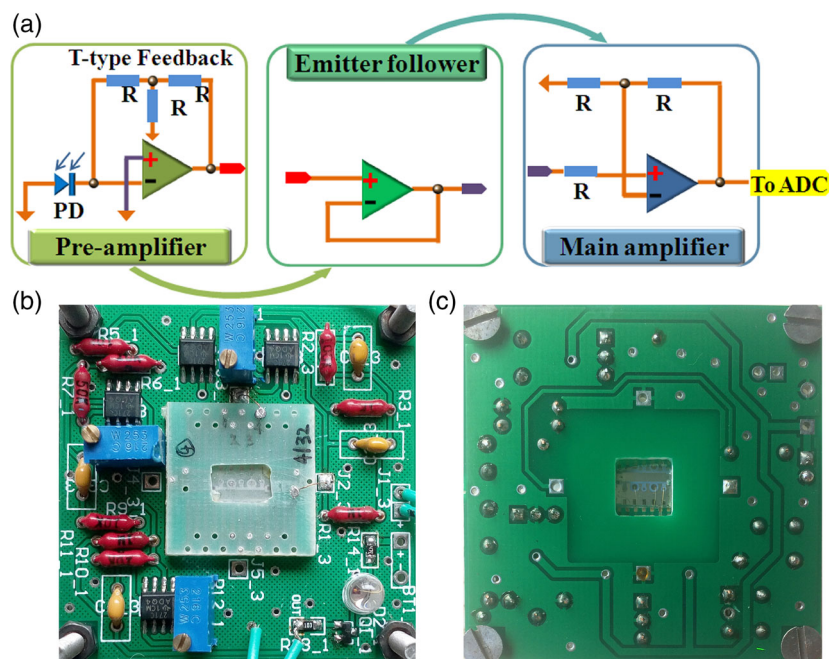


Figure 4. a) The block diagram of signal amplifier circuit for the AlGaIn-based solar-blind UV photodetector; b,c) its whole amplifier circuit in front-side and back-side.

In **Figure 5**, the real-time signal of the AlGaIn-based solar-blind UV photodetector is enlarged by the amplifier circuit and recorded by a commercial data acquisition system. As shown in **Figure 5a,b**, under natural condition without any illumination

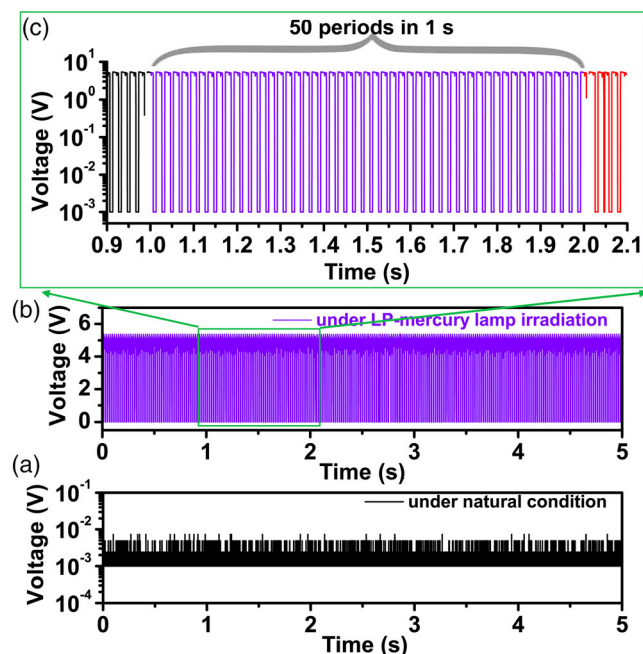


Figure 5. The real-time signal acquisition from the AlGaIn-based solar-blind UV photodetector amplifier circuit. a) Without illumination. b) Illuminated by low-pressure mercury lamp (254 nm). c) A partial enlarged detail of (b) in 1 s.

of a low-pressure mercury lamp (the main spectral line of 254 nm), the amplifier circuit outputs a millivolt-level voltage signal. In comparison, it outputs a voltage signal with maximum amplitude exceeding 5 V under a 2.44 mW cm^{-2} illumination. It should be noted that the 254 nm spectral line of the low-pressure mercury lamp is close to the shortwave cutoff edge of the photodetector. **Figure 5c** shows the partial enlarged detail of **Figure 5b** in 1 s. It contains 50 periods, which is quite in agreement with the operating period of low-pressure mercury lamp using the power frequency of China. In fact, it can output voltage signals of different amplitude depending on the intensity of the incident UV light, as can be seen from the real-time data acquisition video file of the Supporting Information. This means that it can be used as a real-time solar-blind UV radiation sensor for portable equipment if it is highly integrated.

3. Conclusion

In summary, the epitaxy, fabrication, and characterization of a back-illuminated AlGaIn-based solar-blind UV photodetector have been reported in this article. The relatively good electrical and optical performances of the photodetector can be related to crystalline quality improvement and device structure optimization. Based on the photodetector, a discrete signal amplifier circuit is designed to realize real-time solar-blind UV radiation sensing application. The amplifier circuit assembled with the AlGaIn-based solar-blind UV photodetector can output real-time voltage signals of different amplitude depending on the intensity of the incident UV light. This work has a certain guiding significance for the development of a real-time solar-blind UV radiation sensing system.

4. Experimental Section

Epitaxial Growth: The epitaxial growth was implemented on 2 in. double-side polished c-plane sapphire substrates by low-pressure metal-organic chemical vapor deposition (LP-MOCVD). The whole growth process started from the preparation of an AlN template, followed by the epitaxial growth of a polarization-graded AlGa_xN-based solar-blind UV photodetector material. To obtain a high-quality AlN template, a thin MT-AlN layer was introduced to adjust the stress caused by the lattice mismatch after the conventional two-step growth. During the growth, trimethylaluminum (TMAI), trimethylgallium (TMGa), and ammonia (NH₃) were used as Al, Ga, and N precursors, while dicyclopentadienyl magnesium (Cp₂Mg) and silane (SiH₄) were used as p- and n-type dopants. The hydrogen (H₂) was used as the carrier gas in the whole process.

The AlN template consisted of four sublayers, a low-temperature AlN nucleation layer (LT-AlN), a high-temperature/high growth rate AlN layer (HT/HR-AlN), a mesothermal AlN interlayer (MT-AlN), and a high-temperature/low growth rate AlN layer (HT/LR-AlN).^[8] Among them, the LT-AlN layer was grown at 950 °C with a thickness of about 36 nm. The HT/HR-AlN layer with a thickness of 500 nm was grown at 1325 °C with a V/III ratio of 200, a reactor pressure of 4 kPa, and a growth rate of 0.28 nm s⁻¹. A 50 nm-thick MT-AlN layer was grown at 1000 °C with a V/III ratio of 700. For the HT/LR-AlN layer with a thickness of about 200 nm, it was grown at a rate of 0.11 nm s⁻¹ by reducing the source flows under the same conditions of the HT/HR-AlN layer. Followed by ten periods of Al_{0.64}Ga_{0.36}N/AlN (5 nm/5 nm) superlattices (SLs) and a 180 nm-thick intrinsic Al_{0.64}Ga_{0.36}N layer (i-Al_{0.64}Ga_{0.36}N), the polarization-graded AlGa_xN-based solar-blind UV photodetector consisted of a 550 nm-thick Si-doped Al_{0.62}Ga_{0.38}N layer (n-Al_{0.62}Ga_{0.38}N), a 60 nm-thick n-Al_{0.62}Ga_{0.38}N gradient layer with x gradually changing from 0.62 to 0.46, a 300 nm-thick i-Al_{0.46}Ga_{0.54}N layer, and a 100 nm-thick Mg-doped p-Al_{0.46}Ga_{0.54}N gradient layer with its Al-content gradually changing from 0.4 to 0.3 in sequence.

Device Fabrication: Prior to device fabrication, the epitaxial material was rapidly annealed in N₂ atmosphere at 950 °C for 5 min to activate the Mg dopants in the p-Al_{0.46}Ga_{0.54}N layer. Subsequently, the material was patterned by standard photolithography and inductively coupled plasma (ICP) etching, leaving a 500 μm-diameter mesa. The sample was then treated by a photoelectrochemical method to recover the damage made by ICP etching and reduce its leakage current.^[22] Finally, around and on top of the mesa, a ring-like Ti/Al/Ni/Au (30/100/20/200 nm) multilayer electrode and a Ni/Au (30/300 nm) circular electrode were deposited by e-beam evaporation in sequence. The whole device was rapidly annealed under N₂ atmosphere at 700 °C for 60 s to reduce the p- and n-type contact resistances.

Characterization: An in situ optical monitor (LayTec AG) was used to record the in situ growth monitoring curves during growth. The (0002)-plane symmetrical and (10 $\bar{1}$ 5)-plane asymmetrical reciprocal space mapping (RSM) images were measured by an X-ray diffractometer (XRD, Bruker D8). The electrical and optical properties of the photodetector were evaluated by a semiconductor parameter testing system (Agilent B1500A) and a calibrated UV spectral response tester equipped with a 300 W xenon lamp, respectively. The characteristic of transient response was recorded by an oscilloscope (Tektronix DPO 5104 digital oscilloscope) using a 10 mW 266 nm-wavelength Nd:YAG laser as the exciting source. The carrier concentrations in the n-Al_{0.62}Ga_{0.38}N layer and the p-Al_{0.46}Ga_{0.54}N gradient layer were evaluated by an electrochemical analyzer. The carrier concentration for n-Al_{0.62}Ga_{0.38}N was about 2.1×10^{18} cm⁻³, while that for p-Al_{0.46}Ga_{0.54}N gradient layer was slightly changed from inner 2.2×10^{17} cm⁻³ to surface 2.5×10^{17} cm⁻³. The real-time signal acquisition was recorded by a commercial A/D acquisition system.

Supporting Information

Supporting Information is available from the Wiley Online Library or from the author.

Acknowledgements

This work was supported by the Natural Science Foundation of Fujian Province of China (grant no. 2017J01713), and the National Natural Science Foundation of China (grant no. 61504144).

Conflict of Interest

The authors declare no conflict of interest.

Data Availability Statement

Research data are not shared.

Keywords

aluminum gallium nitride, amplifiers, optical signal detection, photodetectors, sensing

Received: May 4, 2021

Revised: July 7, 2021

Published online:

- [1] N. Susilo, S. Hagedorn, D. Jaeger, H. Miyake, U. Zeimer, C. Reich, B. Neuschulz, L. Sulmoni, M. Guttmann, F. Mehnke, C. Kuhn, T. Wernicke, M. Weyers, M. Kneissl, *Appl. Phys. Lett.* **2018**, *112*, 041110.
- [2] M. Kneissl, T. Seong, J. Han, H. Amano, *Nat. Photonics* **2019**, *13*, 233.
- [3] L. G. Innotek, *LG Innotek unveils the world's first '100 mW' UV-C LED*, https://en.prnasia.com/releases/apac/LG-Innotek_Unveils_the_World_s_First_100mW_UV_C-LED-195415.shtml (accessed: November 2017).
- [4] D. Y. Kim, J. H. Park, J. W. Lee, S. Hwang, S. J. Oh, J. Kim, C. Sone, E. F. Schubert, J. K. Kim, *Light Sci. Appl.* **2015**, *4*, 263.
- [5] Z. Zhang, M. Kushimoto, T. Sakai, N. Sugiyama, L. J. Schowalter, C. Sasaoka, H. Amano, *Appl. Phys. Express* **2019**, *12*, 124003.
- [6] S. Zhao, Z. Mi, *IEEE J. Quantum Electr.* **2018**, *54*, 2001009.
- [7] M. Shan, Y. Zhang, T. B. Tran, J. Jiang, H. Long, Z. Zheng, A. Wang, W. Guo, J. Ye, C. Chen, J. Dai, X. Li, *ACS Photonics* **2019**, *6*, 2387.
- [8] Y. Chen, Z. Zhang, G. Miao, H. Jiang, Z. Li, H. Song, *Mater. Lett.* **2020**, *281*, 128638.
- [9] A. Kalra, S. Rathkanthiwar, R. Muralidharan, S. Raghavan, D. N. Nath, *IEEE Photonic Tech. Lett.* **2019**, *31*, 1237.
- [10] R. Yoshizawa, H. Miyake, K. Hiramatsu, *Jpn. J. Appl. Phys.* **2018**, *57*, 01AD05.
- [11] L. Zhang, F. Xu, J. Wang, C. He, W. Guo, M. Wang, B. Sheng, L. Lu, Z. Qin, X. Wang, B. Shen, *Sci. Rep.* **2016**, *6*, 35934.
- [12] Y. R. Chen, Z. W. Zhang, H. Jiang, Z. M. Li, G. Q. Miao, H. Song, *J. Mater. Chem. C* **2018**, *6*, 4936.
- [13] V. Darakchieva, J. Birch, M. Schubert, T. Paskova, S. Tungasmita, G. Wagner, A. Kasic, B. Monemar, *Phys. Rev. B* **2004**, *70*, 045411.
- [14] Y. Hayashi, K. Tanigawa, K. Uesugi, K. Shojiki, H. Miyake, *J. Cryst. Growth* **2019**, *512*, 131.
- [15] A. Kadir, C. C. Huang, K. E. K. Lee, E. A. Fitzgerald, S. J. Chua, *Appl. Phys. Lett.* **2014**, *105*, 232113.
- [16] P. Cantu, F. Wu, P. Waltereit, S. Keller, A. E. Romanov, U. K. Mishra, S. P. DenBaars, J. S. Speck, *Appl. Phys. Lett.* **2003**, *83*, 674.
- [17] M. Leroux, P. Vennéguès, S. Dalmaso, M. Benaissa, E. Feltin, P. De Mierry, B. Beaumont, B. Damlano, N. Grandjean, P. Gibart, *Phys. Status Solidi A* **2002**, *192*, 394.

- [18] Z. Zhang, K. Ding, J. C. Yan, J. X. Wang, Y. P. Zeng, T. B. Wei, Y. Y. Li, B. J. Sun, R. F. Duan, J. M. Li, *Appl. Phys. Lett.* **2010**, 97, 062103.
- [19] J. Simon, V. Protasenko, C. Lian, H. Xing, D. Jena, *Science* **2010**, 327, 60.
- [20] S. Li, M. Ware, J. Wu, P. Minor, Z. Wang, Z. Wu, Y. Jiang, G. J. Salamo, *Appl. Phys. Lett.* **2012**, 101, 122103.
- [21] M. Moseley, A. Allerman, M. Crawford, J. J. Wierer Jr., M. Smith, L. Biedermann, *J. Appl. Phys.* **2014**, 116, 053104.
- [22] H. F. Chen, Y. R. Chen, H. Song, Z. M. Li, H. Jiang, D. B. Li, G. Q. Miao, X. J. Sun, Z. W. Zhang, *Phys. Status Solidi A* **2017**, 214, 1600932.